PCCP

ROYAL SOCIETY OF CHEMISTRY

PAPER

Cite this: *Phys. Chem. Chem. Phys.*, 2021, **23**, 19313

Fabrication and application of composite adsorbents made by one-pot electrochemical exfoliation of graphite in surfactant ionic liquid/nanocellulose mixtures†

Nur Amirah Jamaluddin,[a] Azmi Mohamed, *[ab] Suriani Abu Bakar,[b] Tretya Ardyani,[a] Masanobu Sagisaka,[c] Haruka Saito,[c] Mohamad Hafiz Mamat,[d] Mohd Khairul Ahmad,[e] H. P. S. Abdul Khalil,[f] Stephen M. King,[g] Sarah E. Rogers[g] and Julian Eastoe[h]

Previously, surfactant-assisted exfoliated graphene oxide (sEGO) formed with the triple-chain surfactant TC14 (sodium 1,4-bis(neopentyloxy)-3-(neopentylcarbonyl)-1,4-dioxobutane-2-sulfonate) was applied in wastewater treatment. The extent of dye-removal and the adsorption capacity of the sEGO formed with this triple-chain surfactant outperformed those of two other systems, namely, the di-chain version of TC14 (AOT14; sodium 1,2-bis-(2,2-dimethyl-propoxycarbonyl)-ethanesulfonate) and the single-chain surfactant sodium *n*-dodecylsulfate. In the present study, to further optimise the surfactant chemical structure, the sodium ion of TC14 was substituted with 1-butyl-3-methyl-imidazolium (BMIM) generating surfactant ionic liquids (SAILs; 1-butyl-3-imidazolium 1,4-bis(neopentyloxy)-3-(neopentyloxycarbonyl)-1,4-dioxobutane-2-sulfonate), hereafter denoted as BMIM-TC14. This SAIL, together with nanofibrillated kenaf cellulose (NFC), was used to electrochemically exfoliate graphite, yielding BMIM-TC14 sEGO/NFC composites. These highly hydrophobic polymer composites were then used for the removal of methylene blue (MB) from aqueous solution. ^{1}H NMR spectroscopy was used to elucidate the structure of the synthesised SAILs. The morphologies of the resulting nanocomposites were investigated using Raman spectroscopy, field-emission scanning electron microscopy, and high-resolution transmission electron microscopy. Analysis using small-angle neutron scattering was performed to examine the aggregation behaviour of sEGO and custom-made SAILs. Zeta potential, surface tension, and dynamic light-scattering measurements were used to study the aqueous properties and colloidal stability of the suspension. Amongst the surfactants tested, BMIM-TC14 sEGO/NFC exhibited the highest MB adsorption ability, achieving 99% dye removal under optimum conditions. These results highlight the importance of modifying the hydrophilic moieties of amphiphilic compounds to improve the performance of sEGO/NFC composites as effective adsorbents for wastewater treatment.

Received 19th May 2021,
Accepted 11th August 2021

DOI: 10.1039/d1cp02206g

rsc.li/pccp

Introduction

The removal of organic and inorganic contaminants from wastewater is crucial and necessary to protect and maintain the health of living organisms and their environment. Dyes are amongst the major pollutants[1] generated mostly by the textile industry.[2] Consequently, wastewater containing dyes must be treated before it can be discharged into the environment.

[a] *Department of Chemistry, Faculty of Science and Mathematics, Universiti Pendidikan Sultan Idris, 35900 Tanjong Malim, Perak, Malaysia. E-mail: azmi.mohamed@fsmt.upsi.edu.my*
[b] *Nanotechnology Research Centre, Faculty of Science and Mathematics, Universiti Pendidikan Sultan Idris, 35900 Tanjong Malim, Perak, Malaysia*
[c] *Department of Frontier Materials Chemistry, Graduate School of Science and Technology, Hirosaki University, Bunkyo-cho 3, Hirosaki, Aomori 036-8561, Japan*
[d] *NANO-ElecTronic Centre (NET), School of Electrical Engineering, College of Engineering, Universiti Teknologi MARA, 40450 Shah Alam, Selangor, Malaysia*
[e] *Microelectronic and Nanotechnology – Shamsuddin Research Centre (MiNT-SRC), Faculty of Electrical and Electronic Engineering, Universiti Tun Hussein Onn Malaysia, 86400 Parit Raja, Batu Pahat, Johor, Malaysia*
[f] *School of Industrial Technology, Universiti Sains Malaysia, 11700, Gelugor, Penang, Malaysia*
[g] *ISIS Pulsed Neutron & Muon Source, STFC Rutherford Appleton Laboratory, Harwell Campus, Didcot, Oxfordshire, OX11 0QT, UK*
[h] *School of Chemistry, University of Bristol, Cantock's Close, Bristol, BS8 1TS, UK*
† Electronic supplementary information (ESI) available. See DOI: 10.1039/d1cp02206g

Various methods such as electrochemical reduction, chemical precipitation, oxidation, membrane filtration, ion exchange, and adsorption are commonly used for wastewater treatment.[3] Amongst these, adsorption using highly efficient adsorbents is considered as the most promising and efficient way to remove organic pollutants because it is versatile, fast, simple, and inexpensive.[4] To date, various adsorbents have been tested and modified for their ability to remove pollutants from water and wastewater.[5]

Much research on cationic-dye adsorption has been conducted with graphene oxide (GO), which is a particularly good adsorbent for methylene blue (MB).[6,7] GO can be produced from graphite using various chemical oxidation routes.[8] As a result of oxidation, GO contains numerous oxygen-functionalities including hydroxyl, phenol and epoxy groups on the basal plane and carboxylic acid groups on the edges.[9] These characteristics of GO endow it with an ultra-large specific surface area and negatively charged surface. Hence, the adsorption of cationic dyes onto the GO surface generally occurs through electrostatic interactions.[8,10] Moreover, GO still comprises sp^2-bonded carbon atoms, although the amount is lower than when it is still in the graphite form. Therefore, GO may exhibit π–π interactions with the aromatic moieties of organic dyes.[11] If the organic dyes also bear amino, hydroxyl, and other related groups, they can form hydrogen bonds with the oxygen-containing groups of GO. However, multiple layers of GO are found to aggregate in an aqueous suspension leading to inefficient separation of pollutants from the adjacent aqueous phases.[12] Since GO is a nanomaterial and presents high dispersibility in aqueous solution,[13] its practical applications are hindered: collection of GO sheets is difficult after adsorption, meanwhile, the unprecipitated GO may lead to potential nanotoxicity[14] to aquatic creatures. These problems restrict large-scale practical applications of GO as adsorbents. Compared to our previous findings, the recovery of GO after scavenging pollutants would be improved by making composites.[15]

For these reasons, a wide range of GO-based adsorbents have been developed over recent years, such as GO-based aerogels[12] and composites.[16] Thus, a combination of exfoliated graphene oxide and nanocellulose to make a hybrid material is seen as the most viable option to suit these needs. Cellulose can act as a substrate[12] for GO and help form stable adsorbent structures.

Nanofibrillated kenaf cellulose (NFC) is extensively used as an adsorbent in dye wastewater treatment because it contains large proportions of intra- and inter-molecular hydrogen bonds and has a high porosity.[17–19] This biomaterial has the advantages of non-toxicity and biocompatibility.[20] Incorporating GO into nanocellulose is suitable for the preparation of hybrid materials. To ensure dissolution and compatibility with other materials, nanocellulose are typically treated with acids, bases, surfactants, and ionic liquids (ILs).[21–23] Meanwhile, a number of works have highlighted the compatibility of surfactant and ILs with graphitic materials.[24,25] ILs possess very low vapour pressures, high polarities, and good thermal stabilities.[26,27] Additionally, the high dielectric constants of ILs prevent GO stacking caused by van der Waals interactions.[28,29] All these properties render ILs suitable for applications involving GO.

Amongst various routes that have been developed to synthesise GO, surfactants and ILs are usually used in the electrochemical exfoliation of graphite. Initially, graphene consists of a graphitic sp^2-conjugated carbon structure. After oxidation, the disruption of the π-conjugation of the graphitic structure occurs, causing defects with sp^3-carbon domains forming GO.[30] The electrochemical exfoliation of graphite primarily involves intercalation of ions which increases the interlayer spacing between the graphene sheets (in bulk graphite). The setup for exfoliation generally comprises an electrolyte (*e.g.*, surfactant solution), electrodes (can be graphite for both electrodes), and a power supply.[31] Surfactants increase the interlayer distances of the graphene layers in the graphite electrodes, and hence facilitate the exfoliation of the sheets. Surfactants undergo adsorption and desorption at interfaces spontaneously over the microsecond to second timescales,[32,33] which is an important aspect for exfoliation of graphite. Larger particles such as GO require a higher energy input to enhance colloidal stability,[34] thereby providing adsorption sites for MB.

Our previous study successfully used electrochemically produced GO assisted by commercial and custom-made surfactants.[15] The resulting surfactant/GO dispersions can be directly used for MB adsorption studies.[15] Earlier, the common surfactant sodium *n*-dodecylsulfate (SDS) had been used for the production of exfoliated graphene and subsequently applied in MB removal from aqueous solution.[35] Later, GO–IL composites were successfully synthesised using the Tour method, combined with 1-tetradecyl l,3-butylimidazolium IL. These highly hydrophobic composites have been used for the adsorption of sulfamethoxazole and reactive blue 19, and the adsorption capacities were 27.25 and 416.7 mg g^{-1}, respectively.[36] Graphene exfoliation by SAILs has also been achieved.[27] The micellisation of short-chain ILs such as $[C_4mim][BF_4]$ leads to aggregation in aqueous environments.[37,38] It was shown that imidazolium-based ILs have better surface-active properties compared with analogous common ionic surfactants.[39] Therefore, fabricating IL surfactant GO/cellulose-based adsorbents could provide new approaches for wastewater treatment. Developing a one-pot approach that combines the simplicity of electrochemical exfoliation and the compatibility of amphiphiles with GO and nanocellulose represents a convenient approach for developing GO/nanocellulose adsorbents. To the best of our knowledge, such a system has not yet been reported. It is also interesting to explore how the modification of surfactant headgroups affects the stability of GO dispersions and the adsorption capacity of the resulting nanocomposites.

Extending previous work,[15] the present study uses the same fabrication method but with the addition of nanofibrillated cellulose to the electrolyte mixture to obtain nanocomposite adsorbents. Graphite was directly exfoliated in the surfactant or SAILs and NFC dispersions to obtain the nanocomposites. To investigate the effectiveness of the composites as organic dye adsorbents, batch-adsorption studies using MB as a model

pollutant were conducted. The effectiveness of a range of composites was measured in terms of the adsorption capacity and extent of dye removal. Additionally, the adsorption behaviour of the prepared composites was investigated in term of adsorption isotherms and kinetics. Here, the adsorption parameters were initial dye concentration and adsorption contact time. Following previous works, and to provide a comparable study, other adsorption parameters such as solution pH, adsorbent dosage, temperature, and shaker speed were set to be constant.[15] Significantly, the present study examines the surfactant headgroup effects by exchanging the small sodium ion for the bulkier imidazolium ion. The results also highlight the relationship of surfactant structure–nanocomposite performance for the development of stabiliser/GO/nanocellulose dye adsorbents.

Materials and methods

Materials

Sodium *n*-dodecylsulfate (SDS) was purchased from Sigma-Aldrich and used as received. 1-Butyl-3-methyl-imidazolium chloride (Merck, 99%) was used without further purification. The surfactants TC14, AOT14, BMIM-DS, BMIM-AOT14, and BMIM-TC14 (chemical structures are shown in Table 1) were custom-made and synthesised following previous works.[40–42] Nanofibrillated kenaf cellulose (NFC) was received from the Forest Research Institute Malaysia. All aqueous solutions were prepared with ultrapure deionised (DI) water. High-purity graphite (99.9%) rods (Model MV10) were used as received. Detailed surfactant characterisation is given in the ESI.†

Preparation of surfactant or SAIL sEGO/NFC composites

The electrolytes were prepared by mixing 0.05 M surfactant or SAIL solution (50 mL) with 2.5 g of NFC. The mixtures were vigorously stirred for 2 h until stable dispersions formed. The anode and cathode for the exfoliation process were high-purity graphite rods with a diameter of 10 mm and length of 150 mm. Electrochemical exfoliation was conducted at ambient temperature with a power supply as the electrical source for 24 h. The voltage was set to be constant at 7 V. Once the process was completed, the dispersions were then subjected to stirring and sonication for 1 h, resulting in a uniform dispersion of sEGO/NFC. The mixtures was then cast in a Petri dish (as a mould) and left to dry overnight in an oven at 50 °C. The sEGO/NFC composites were obtained by peeling the films from the Petri dishes. The composite samples were denoted as surfactant or SAIL sEGO/NFC.

Batch-adsorption studies

To evaluate the adsorptive capacity of the surfactant or SAIL sEGO/NFC composites towards MB, experiments were conducted under the optimum conditions following our previous work: pH 7, temperature of 22.5 °C, and 5 mg of surfactant or SAIL sEGO/NFC composite.[15] About 5 mg of the composites was placed in 50 mL Erlenmeyer flasks containing 25 mL of MB solutions with different initial concentrations (5–15 ppm). The dye solution–sEGO/NFC mixture was then placed on an orbital shaker for 15–1440 min to reach equilibrium. The supernatant was then analysed using a spectrophotometer (UV Cary 60, Shimadzu, Japan) at an absorption wavelength of 664 nm to determine the final dye-solution concentrations. All experiments were conducted in triplicate under identical conditions unless otherwise stated.

Surfactant or SAIL sEGO/NFC morphology characterisation

The morphology of all surfactant or SAIL sEGO/NFC composites were observed using a field-emission scanning electron microscope (FESEM) (Hitachi SU8020) and a high-resolution transmission electron microscope (HRTEM) (JEOL 2100F). The FESEM images were taken at a working distance of 8 mm using an upper detector with 2 and 5 kV accelerating voltages. The composites were cryo-sectioned using a diamond knife prior to HRTEM imaging. A Renishaw InVia micro Raman spectrophotometer with argon ion-laser source at a wavelength of 514 nm was used to study the structural changes of graphite and GO, if any.

Zeta (ζ) potential measurements

The sEGO surface charge was determined through zeta-potential measurements (Photal OTSUKA ELECTRONICS ELSZ-1000 zeta potential and particle size analyser) by using the Smoluchowski equation and single-peak Lorentz fitting. Measurements were performed in a flow cell with a 400 μs sampling time, cumulative number of 7, 15° measuring angle, 50 μm pin hole size, and 70.000 cm^{-1} cell constant at 25 °C. The zeta-potential calculation was performed based on the properties of the aqueous mixtures: refractive index 1.3328, viscosity 0.8878 cP, and relative permittivity 78.3 F m^{-1}. For each sample, measurements were performed 10 times, and the average zeta potential was taken.

Dynamic light-scattering (DLS) measurements

DLS was used to determine the particle size of surfactants and surfactants/sEGO using a DLS/SLS-5000 instrument (ALV, Langen) with a He–Ne laser (632.8 nm, 22 mW) at a scattering angle of 90°. The measurements were conducted in triplicate with values averaged to obtain the particle size.

Small-angle neutron scattering (SANS) measurements

Small-angle neutron scattering studies were conducted using a time-of-flight diffractometer LOQ instrument (ISIS Pulsed Neutron & Muon Source, UK). The incident neutron wavelengths of λ = 2.2–10 Å at 25 Hz frequency gave an accessible Q range of 0.007–0.23 $Å^{-1}$. Deuterium dioxide was used as the SANS sample solvent background to improve the signal-to-noise and neutron contrast. The samples were contained in 2 mm-path-length quartz cells held in a thermostatted sample-changer at 25 °C. Absolute scattering intensities $I(Q)$ (cm^{-1}) were determined to be within 5% by measuring the scattering from a partially deuterated polymer standard with a known molecular weight, and so $I(Q = 0)$. The Mantid framework

Table 1 Surfactants used in this study

Surfactant name	Surfactant structure and name
SDS	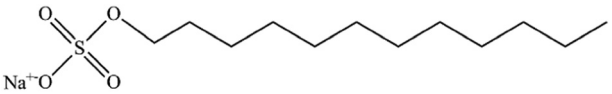 sodium *n*-dodecylsulfate
AOT14	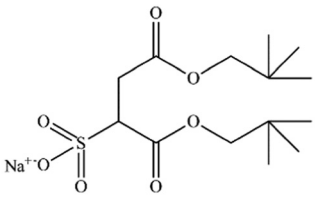 sodium 1,2-bis-(2,2-dimethyl-propoxycarbonyl)-ethanesulfonate
TC14	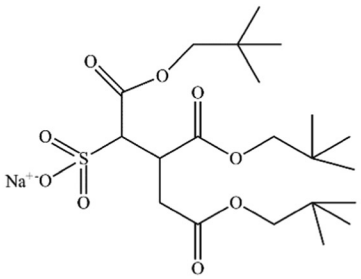 sodium 1,4-bis(neopentyloxy)-3-(neopentyloxycarbonyl)-1,4-dioxobutane-2-sulfonate
BMIM-DS	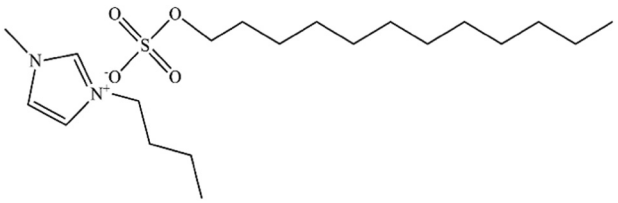 1-butyl-3-methyl-imidazolium dodecylsulfate
BMIM-AOT14	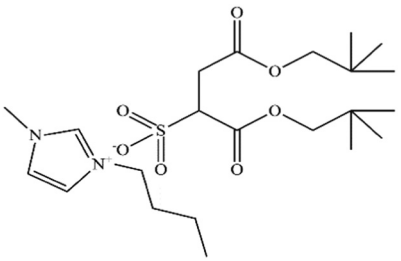 1-butyl-3-imidazolium 1,2-bis-(2,2-dimethyl-propoxycarbonyl)-ethanesulfonate
BMIM-TC14	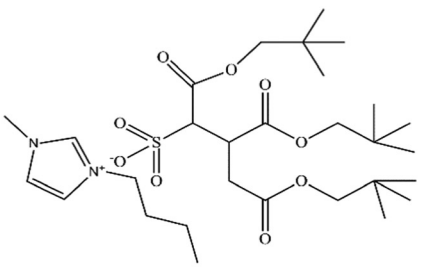 1-butyl-3-imidazolium 1,4-bis(neopentyloxy)-3-(neopentyloxycarbonyl)-1,4-dioxobutane-2-sulfonate

(www.mantidproject.org) was used to obtain instrument-independent reduced SANS data which were then model-fit using the SasView program (www.sasview.org) constraining scattering length densities and other known parameters. Unknown structural parameters were allowed to 'float' throughout the fitting process to obtain an optimised fit as required by different scattering model functions. The SANS data were presented as a function (magnitude) of the scattering factor, $Q = (4\pi/\lambda)\sin(\theta)$, where θ is half of the scattering angle. Thus, the approximate size of a feature is $2\pi/Q$.

Surface tension measurements

A Willhelmy tensiometer (CBVP-A3, Kyowa Interface Science) equipped with a platinum plate was utilised to determine the air–water (a/w) surface tension of surfactant solutions and sEGO systems. All measurements were conducted at 25 °C until the surface tension reached a constant value to avoid dynamical relaxation effects. The critical micelle concentrations (CMCs) of surfactants and sEGOs were obtained from the intersection of surface tension (γ) *versus* ln of concentration ($\ln c$) plot.

Results and discussion

Adsorption studies: removal percentage and adsorption capacity

The percentage removal (%) of MB and MB-adsorption capacity on the surfactant or SAIL sEGO/NFC composites were determined using eqn (1) and (2), respectively.

$$R\% = \left(\frac{C_0 - C_e}{C_0}\right) \times 100 \quad (1)$$

$$q_e = \frac{(C_0 - C_e)V}{W} \quad (2)$$

where C_0 is the initial MB concentration (mg L^{-1}), C_e is the equilibrium MB concentration (mg L^{-1}), q_e is the amount of MB adsorbed per gram adsorbent (mg g^{-1}), V is the volume of the solution (L), and W is the mass of the adsorbent (g). Fig. 1 compares MB removal by using blank NFC and surfactant or SAIL sEGO/NFC composites. The effectiveness of the sEGO/NFC composites in this application follows the trend BMIM-TC14 > TC14 > BMIM-AOT14 > AOT14 > BMIM-DS > SDS (Table 2). The removal efficiency of MB increased by 65% (compared with that of blank NFC sample) when using BMIM-TC14 sEGO/NFC, which performed best. In general, the SAIL sEGO/NFC composite offered higher MB removal by nearly 3–8% compared to the surfactant sEGO/NFC samples. The surfactant or SAIL sEGO/NFC composites used in this study did not achieve higher removal efficiency or adsorption capacity compared with other works (Table 2). However, it was shown that significant dye removal can be obtained at a considerably lower sEGO/NFC composite content (5 mg).

Owing to π–π interactions, GO is easily aggregated and poorly dispersed.[43] Thus, the adsorbed surfactants, acting as stabilisers, prevent the agglomeration of adjacent sEGO by weakening the van der Waals interactions.[15] Surfactant layers

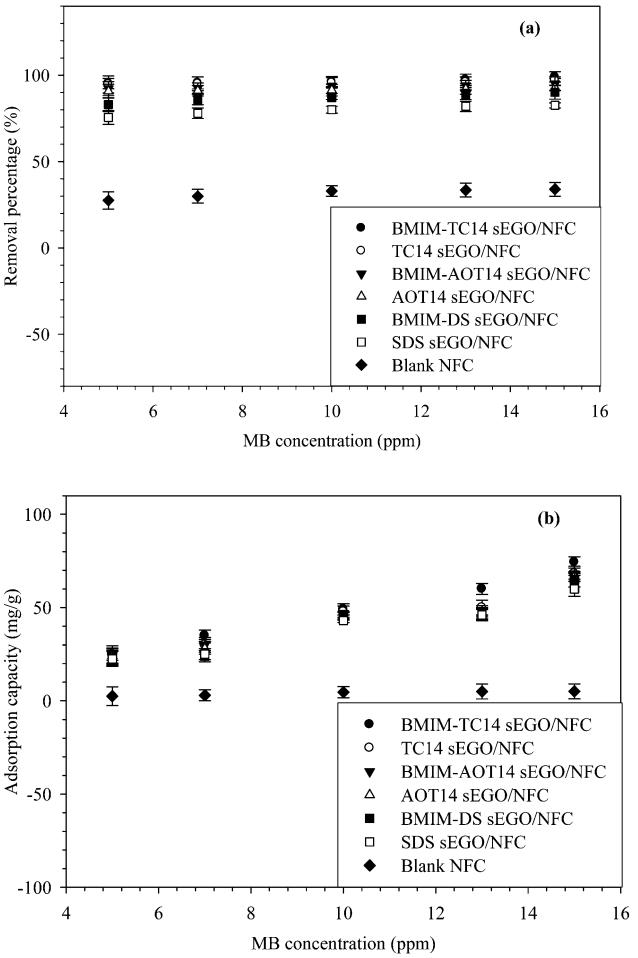

Fig. 1 Removal (a) and adsorption capacity (b) of MB by surfactant or SAIL sEGO/NFC composites at equilibrium dye concentration with 1440 min contact time. The error bars represent the standard deviation (n = 3).

covering the GO surfaces affect the total negative surface charge. According to Wang *et al.*,[43] the adsorption capacity of the GO/CNF composite is eight times higher than that of pure CNF, comparable to this study. The low adsorption capacity of pure cellulose was due to the weak interactions between MB and cellulose chains. They proposed that the underlying reason for the higher adsorption capacity of GO/cellulose than pure cellulose was the abundant hydroxyl groups, *e.g.*, the C═O and C═C groups from both materials form strong interactions with the organic pollutant.

Effect of initial MB concentration

The initial concentration of the MB solution has a significant effect on its removal. As expected, the addition of sEGO inside the NFC matrix led to an enhancement in the adsorption capacity of NFC itself (Fig. 1). Upon adding sEGO, the capacity of NFC, which was previously very low (5 mg g^{-1}), increased and reached 74.3 mg g^{-1} in the BMIM-TC14 sEGO/NFC composite. The adsorption capacity of BMIM-TC14 sEGO/NFC was approximately 15 times larger than that of blank NFC. Looking at the very low adsorption capacity of blank NFC (Fig. 1b), the

Table 2 Comparison of the adsorption capacities of various reported adsorbents based on graphene oxide composite for MB

Adsorbent[a]	Source & method	W^b (mg)	Removal (%)	$q_e{}^c$ (mg g^{-1})	$C_0{}^d$ (ppm)	pH	T^e (K)	t^f (min)	Ref.
BMIM-TC14 sEGO/NFC	Electrochemical exfoliation & *in situ* method	5	99	74	15	7	296	1440	This study
TC14 sEGO/NFC		5	97	68	15	7	296	1440	This study
BMIM-AOT14 sEGO/NFC		5	95	68	15	7	296	1440	This study
AOT14 sEGO/NFC		5	92	67	15	7	296	1440	This study
BMIM-DS sEGO/NFC		5	90	65	15	7	296	1440	This study
SDS sEGO/NFC		5	83	60	15	7	296	1440	This study
CGO	Modified Hummers' method and wet-spinning technique	20	—	383	160	6	298	50	14
GO/CNFs	Modified Hummers' method, easy blending and freeze-drying process	20	98	44	50	—	—	350	43
Chitosan/CMC/GO	Hummers' Method, vacuum filtered and hot-air oven process	100	100	122	10	7	303	180	44
RCE/GO	Hummers' method, solution mixing-regeneration and freeze-drying process	50	99	68	20	6	298	30	45

[a] CGO = cellulose/GO. CNF = cellulose nanfibrils. CMC = carboxymethyl cellulose. RCE = regenerated cellulose. [b] Adsorbent dosage. [c] Adsorption capacity. [d] Initial dye concentration. [e] Temperature. [f] Contact time.

adsorption-capacity enhancement of the composites led to sEGO dispersion. The presence of a higher amount of oxygen-functionalised groups from the stabiliser and GO on the composite was presumed to enhance the adsorption capacity of the NFC. To investigate whether the presence of surfactant in sEGO affected the adsorption capacity, adsorption studies with surfactants alone were also conducted. The results (Fig. S7, ESI†) showed that the removal was negligible (less than 1%). Therefore, the enhancement was largely due to GO and the surfactants primarily helped GO to be stably and uniformly dispersed inside the NCF matrix.

The amounts of adsorbed MB per unit mass of the adsorbent are shown in Fig. 1b. The adsorbed amount increased with increase in surfactant chain branching. As the initial MB concentration increased, the adsorption capacity of MB increased, consistent with the increase in the contact between MB and the active sites in the surfactant or SAIL sEGO/NFC composite. The adsorption capacity tended to be constant when the initial MB concentration was higher than 10 ppm. Interestingly, when the initial concentration of MB was lower, the percentage removal was higher. The driving forces of concentration gradient and the diffusion of MB dye into the sEGO composite increased with increase in dye concentration. The MB-adsorption capacity of the sEGO composites increased concomitantly with increase in dye concentration until the equilibrium state was achieved (Fig. 1b). The higher adsorption capacity of the surfactant or SAIL sEGO/NFC composite compared with that of blank NFC could be explained by the electrostatic and π–π interactions of the surfactant or SAIL sEGO/NFC surface with dye molecules. Considering the hexagonal lattice of graphene, the sEGO/NFC composites can link with the aromatic structure of MB. Besides, surfactant or SAIL sEGO/NFC composites have negatively charged groups (from the oxygenated groups of GO), which could link with the $-N(CH_3)^+$ groups of MB,[43] thus increasing the adsorption capacity.

Effect of contact time

Contact time strongly affects the adsorption equilibrium process and is crucial for practical applications. Obviously, the removal rate of MB by all surfactant or SAIL sEGO/NFC composites was rapid and adsorption reached equilibrium within 1440 min, as shown in Fig. S8 (ESI†). More than 70% removal of MB from aqueous solution was achieved within the initial 5 min of adsorption. Most dye rapidly adsorbed in the first 15 min and reached equilibrium at approximately 60 min. The MB removal by the composites *via* adsorption rose rapidly at the beginning and gradually slowed down until equilibrium. This finding may be explained by the large number of available adsorption sites at the initial stage. However, with prolonged contact time, the number of active sites decreased owing to a steric barrier between the adsorbed dye molecules on the surface of the composite and solution phase.[46] During dye adsorption, dye molecules initially approached the adsorbent surface and finally diffused into the internal structure. Fig. S8 (ESI†) shows that the curves were single, smooth, and continuous, leading to saturation, suggesting the possible monolayer coverage of MB on the GO surfaces.[46]

Adsorption-isotherm study

To further understand the adsorption behaviour and equilibrium data, adsorption isotherms were studied and are plotted in Fig. S5 (ESI†). These isotherms can describe the relationship between the adsorbent and adsorbate when the equilibrium state is reached. This information is crucial to optimise the use of adsorbents. In this study, two of the most widely applied

isotherm models, *i.e.*, the Langmuir and Freundlich models, were used to describe the amount of MB adsorbed and its equilibrium concentration. The Langmuir isotherm is based on the following assumptions: (1) adsorption occurs on a homogeneous adsorbent surface having identical sites with equivalent availability and energy, (2) localised adsorption, as no interaction occurs between neighbouring adsorbate molecules, and (3) each active site can interact with only one adsorbate molecule.[47] The linear form of the Langmuir model can be expressed as follows:

$$\frac{1}{q_e} = \frac{1}{q_{max}} + \frac{1}{q_{max} K_L C_e} \quad (3)$$

where q_e (mg g^{-1}) is the dye-adsorption capacity at equilibrium, C_e (mg L^{-1}) is the equilibrium concentration of the dye in the solution, q_{max} is the maximum dye-adsorption capacity, and K_L (L mg^{-1}) is the Langmuir constant corresponding to the adsorption energy that can be obtained from plotting C_e/q_e *versus* C_e. Meanwhile, the dimensionless separation factor equilibrium parameter R_L (which indicates the shape of the isotherm) is used to determine whether the adsorption is 'favourable' or 'unfavourable'. R_L can be defined as follows:

$$R_L = \frac{1}{1 + k_L C_0} \quad (4)$$

where C_0 (mg L^{-1}) is the initial MB concentration. The value of $R_L = 0$ indicates irreversible adsorption, whereas $R_L = 1$ means linear behaviour. Favourable adsorption is indicated by R_L values between 0 and 1 ($0 < R_L < 1$). The adsorption is unfavourable if $R_L > 1$.

The Freundlich isotherm assumes that the adsorbate adsorbs onto a heterogeneous adsorbent surface. The adsorption energy exponentially decays along with increase in surface-coverage and is thus more suitable to describe a non-ideal multilayer adsorption.[48] The model can be written as follows:

$$\log q_e - \log K_F = \frac{1}{n} \log C_e \quad (5)$$

where K_F represents the Freundlich isotherm constant whilst n is the dimensionless heterogeneity parameter, an estimation of adsorption intensity. As such, n and K_F can be determined through the slope and intercept of the linear plot of $\log q_e$ *versus* $\log C_e$, respectively.

In the present study, MB adsorption into BMIM-TC14 sEGO/NFC fitted the Langmuir and Freundlich isotherms with correlation coefficients (R^2) of 0.94 and 1.00, respectively. The surface of the BMIM-TC14 sEGO/NFC composite may be homogeneous or heterogeneous, so the adsorption of MB occurred either through monolayer or multilayer adsorption. The dimensionless value (R_L) for BMIM-TC14 sEGO/NFC was found to be 0.94, indicating that adsorption was favourable. The rest of the samples were best described by the Freundlich isotherm with R^2 values >0.9. The values of R_L corresponding to the initial concentration of 15 ppm of MB for all surfactant or SAIL sEGO/NFC composites are listed in Table S6 (ESI†). The adsorption of MB onto the sEGO/NFC composites is apparently favourable because R_L was found between 0 and 1. This finding implied strong interactions between MB and the surfactant or SAIL sEGO/NFC composites.

Adsorption kinetics

Studies on kinetics are important to predict the adsorption equilibrium time, the adsorption behaviour, and the interaction between the MB dye and surfactant or SAIL sEGO/NFC composites. The adsorption kinetics of MB onto sEGO was examined at five initial MB concentrations (5, 7, 10, 13, and 15 ppm). To analyse the adsorption behaviour, we used the pseudo-first- (eqn (6)) and pseudo-second-order (eqn (7)) models.[49] The linear forms of the aforementioned kinetic models are given as follows:

$$\log(q_e - q_t) = \log q_e - k_1 \times t \quad (6)$$

$$\frac{t}{q_t} = \frac{1}{k_2 \times q_e^2} + \frac{t}{q_e} \quad (7)$$

where q_t and q_e are the adsorption capacities of the adsorbents (mg g^{-1}) at t time and equilibrium, respectively; k_1 represents the pseudo-first-order rate constant (min^{-1}) and t is the contact time (min). The plot of $\log(q_e - q_t)$ *versus* t gives a linear relationship where the values of q_e and k_1 can be determined from the intercept and slope of the plot, respectively. As for eqn (7), k_2 (g mg^{-1} min^{-1}) represents the pseudo-second-order rate constant. The equilibrium sorption capacity q_e and k_2 can be obtained from the slope and intercept of the linear plot of t/Q_t *versus* t, respectively. Table S6 (ESI†) summarises the parameters and linearity of the pseudo-first-order and pseudo-second-order models. The analyses showed that MB adsorption obeys a pseudo-second-order model. The coefficient of determination (R^2) was used to evaluate the models.

Comparison of the correlation coefficient (R^2) between the two kinetic models gave higher R^2 for the pseudo-second-order (>0.9) than the pseudo-first-order (<0.9) for all SAIL sEGO/NFC samples. This finding indicated that the adsorption mechanism of MB by SAIL sEGO/NFC is better described by the pseudo-second-order model, whereby the uptake of MB is second-order with respect to the available SAIL sEGO/NFC sites. Meanwhile, the kinetic behaviour of the composites stabilised with various sodium surfactants (TC14, AOT14, and SDS sEGO/NFC) was well described by the pseudo-first and pseudo-second kinetic models, having R^2 values higher than 0.9. The results also implied that MB adsorption onto the adsorbent may involve chemical adsorption. According to Vincent *et al.* (2014), small particle sizes yield larger k_2 values because of reduced intraparticle diffusion resistance.[50] A higher k_2 value also reflects a shorter time required for MB to be adsorbed onto the surfactant or SAIL sEGO/NFC surfaces. Therefore, the surfactant or SAIL sEGO/NFC composites can be deemed as efficient adsorbents in terms of the time required for MB removal.

The value of k_1 can be used to evaluate the electrostatic attraction between positive MB molecules and the negatively charged sEGO surface. According to Tan & Hameed (2017),

$1/k_1$ is the time scale for the adsorption process to reach equilibrium; a longer time (smaller k_1) is needed if the initial concentration (C_0) is larger.[51] Another report has claimed that a small particle size is associated with large values of k_1.[50] A higher k_1 value reflects greater electrostatic attraction between adsorbate and adsorbent. Although a significant maximum adsorption capacity (q_e) difference existed between composites that obeyed the pseudo-first-order model (*i.e.*, TC14, AOT14 and SDS sEGO/NFC composites), the value of k_1 for the mentioned samples was very similar. Hydrophobicity may have contributed to adsorption, but considering the molecular structure of EGO and MB, the electrostatic interaction may have been the predominant force controlling MB adsorption onto sEGO.

Morphology of surfactant and SAIL sEGO/NFC composites

The FESEM images of blank NFC and surfactant or SAIL sEGO/NFC composites are presented in Fig. 2. Fig. 2(a and a′) show that NFC has a homogeneous and smooth surface. By contrast, the FESEM images of sEGO/NFC composites displayed rougher surfaces and more pronounced bumps. This finding may be due to the presence of sEGO clusters corresponding to the potential adsorption sites. The representative FESEM images of the composites (g and g′) clearly demonstrated that the fibril cellulose matrix contained a characteristic two-dimensional plane of GO sheets.[52,53] The lamellar structure of GO offers a high surface area, which benefits dye adsorption.[54] Exfoliated sheets of sEGO indicated the successful oxidation and exfoliation. The characteristics of GO such as smooth surfaces, wrinkled ripples, and thin layers were also observed in the FESEM image.[36] Comparing the morphology of SDS, AOT14, and SDS sEGO/NFC with those of the SAIL sEGO/NFC composites, the one with less sEGO had folded stacked layers with a bulkier form of GO. Meanwhile, SAIL sEGO/NFC exhibited less stacked sheets and higher exfoliated GO dispersed in the NFC matrix. The improved dispersibility and exfoliation in composite containing GO stabilised by SAILs may have enhanced the adsorption capacity.

The rough surface, thin layered sheets, and good GO distribution of BMIM-TC14 sEGO/NFC sample could offer more adsorption sites owing to a larger surface area. All thin multilayered sheets had random folds, formed through hydrogen-bond interactions of the oxidation groups and the π–π stacking of aromatic skeletons.[55] The wrinkles the of GO sheets resulting from the repulsive negative charges of the deprotonated carboxylic acid groups are more pronounced in the higher-magnification FESEM image (Fig. 2e).[56] Overall, the choice of stabiliser may have affected the degree of exfoliation of GO and its dispersibility, as well as the adsorption capacity of the composites. Fig. 3 shows the HRTEM images of the BMIM-TC14 sEGO/NFC composite.

Under HRTEM observation, the composite had an opaque appearance, indicating the presence of GO. The darker region of the image corresponded to the sEGO embedded in the NFC composite. The enlarged view (Fig. 3c) revealed that sEGO had a needle-like structure and existed as a multilayer of GO.[25] These results confirmed that graphite was successfully exfoliated to obtain GO sheets.

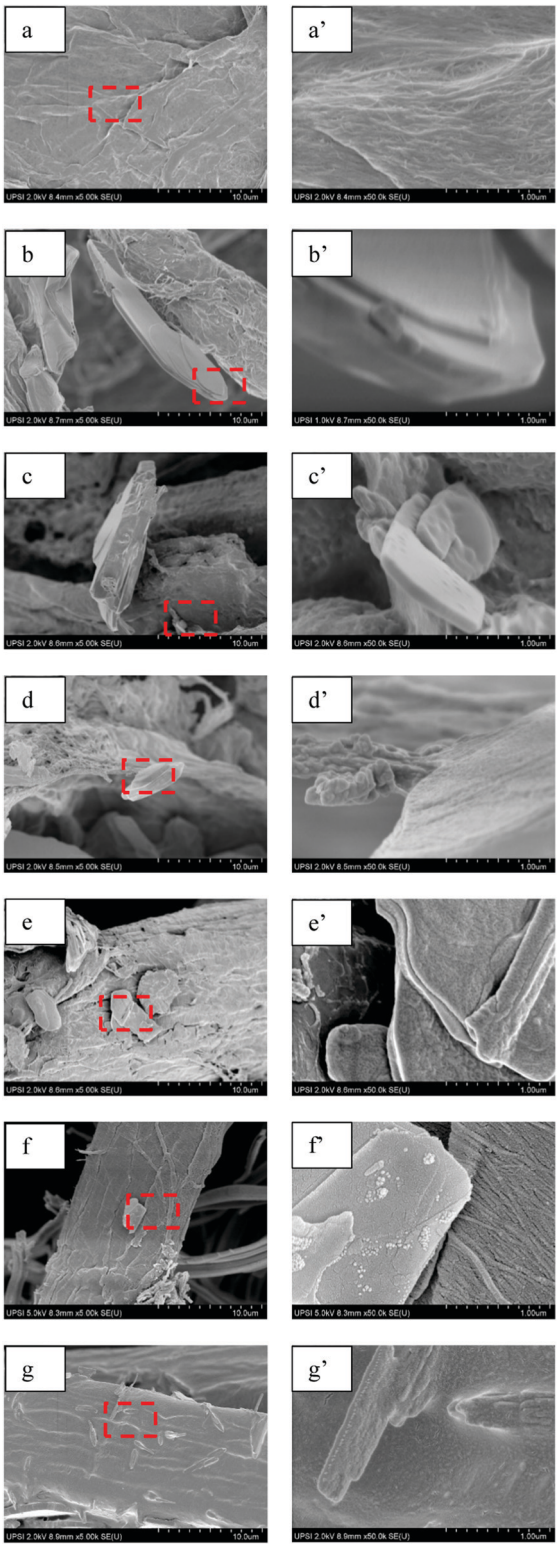

Fig. 2 FESEM images of NFC (a and a′), SDS sEGO/NFC (b and b′), AOT14 sEGO/NFC (c and c′), TC14 sEGO/NFC (d and d′), BMIM-DS sEGO/NFC (e and e′), BMIM-AOT14 sEGO/NFC (f and f′), and BMIM-TC14 sEGO/NFC (g and g′).

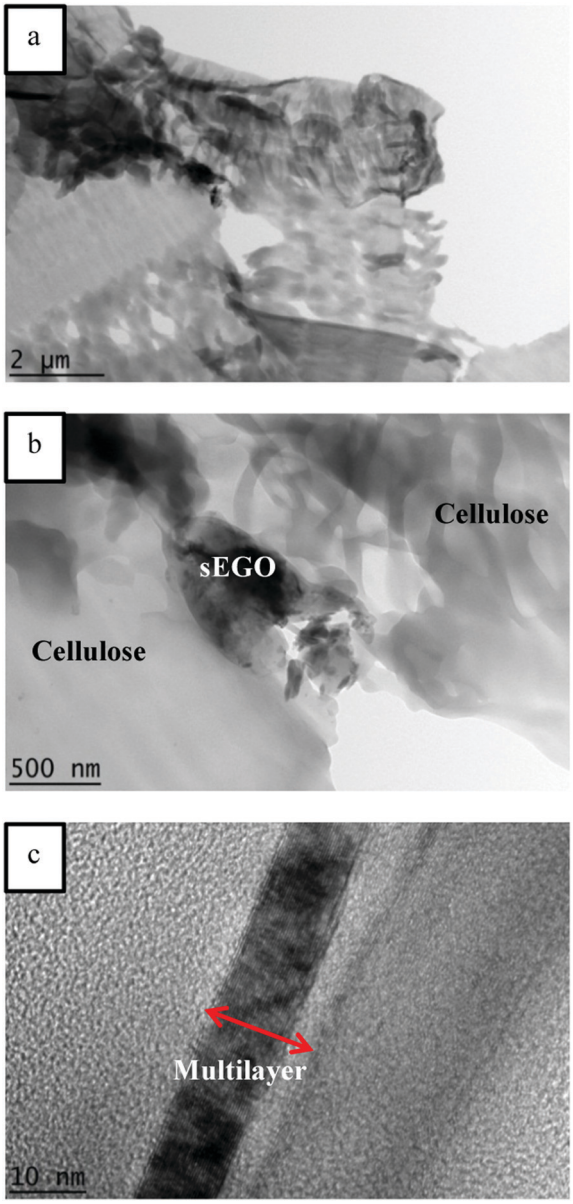

Fig. 3 HRTEM images of BMIM-TC14 sEGO/NFC composite.

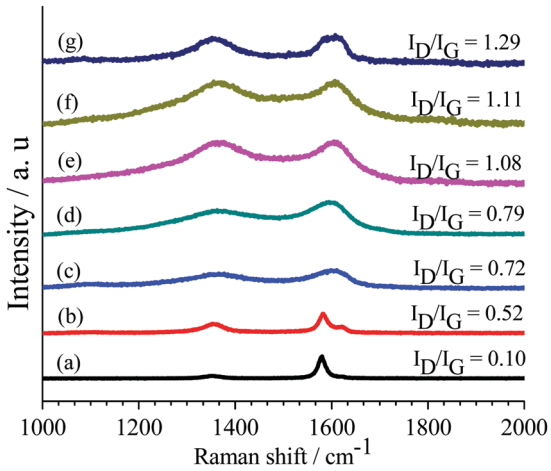

Fig. 4 Raman spectra of graphite (a), SDS/sEGO/NFC (b), AOT14/sEGO/NFC (c), TC14/sEGO/NFC (d), BMIM-DS/sEGO/NFC (e), BMIM-AOT14/sEGO/NFC (f), and BMIM-TC14/sEGO/NFC (g).

Raman spectroscopy

Fig. 4 shows the Raman spectra of graphite and surfactant or SAIL sEGO/NFC composites. The two prominent peaks of GO can be observed. The D-peak was attributed to a defect-related band, whereas the G-peak was related to the sp^2 networks of the carbon atoms.[57] The calculated Raman intensity ratio (I_D/I_G) is generally used as a quantitative measure of the disorder structure of carbon nanomaterials, with higher ratios indicating higher defects in the carbon structure.[55] The appearance of the D-peak of different intensities in all spectra confirmed successful exfoliation.[58] The small and weak D-peak of the graphite spectrum (I_D/I_G = 0.10) indicated the absence of defects and disordered structure. Results (the I_D/I_G ratio of graphite being lower than that of the composites) indicated that the size reduction of the in-plane sp^2 domains was due to oxidation and exfoliation. Broad and strong G-peaks with an I_D/I_G ratio of 0.7–1 indicated significant edges rather than basal defects in the surfactant or SAIL sEGO/NFC composites as a result of ultrasonication.[59]

The I_D/I_G ratio for all surfactants and SAIL sEGO/NFC composites was found to be higher than that of pristine graphite, suggesting the possible electronic interaction between anionic surfactants and GO sheets[60] (Fig. 4). This finding implied the successful incorporation of anionic surfactant molecules onto the GO surfaces. The intensity ratio of the D-peak to G-peak (I_D/I_G) changed from 0.95 to 1.24, indicating decreased average size of the in-plane sp^2 domains[61] and increased disordered graphene sheets owing to the addition of anionic surfactants. Furthermore, the intensity ratio (>0.5) for all surfactants and SAIL sEGO/NFC samples suggested that the surface of the sEGO composites was decorated by abundant oxygen-containing functional groups from the anionic surfactants. The presence of these oxygenated groups improved the hydrophilicity of the sEGO composites, which was advantageous for dye adsorption.[45] The higher G-peak intensity for all composite samples suggested the complete intercalation of surfactant and GO[62] along with cellulose.

Zeta potentials

Zeta potential is an important indicator to predict and control the stability of a colloidal system. The zeta (ζ)-potential measures the potential difference between the mobile particles (sEGO) and dispersant (surfactant) at the hydrodynamic slipping plane under an electric field.[63–65] Zeta-potential measurements indicated that these suspensions were electrostatically stabilised by negative charges, possibly from the carboxylated groups of GO that are believed to decorate the periphery of the GO lamellae.[66] A thick and stable surfactant or SAIL 'film' formed around the sEGO particles, leading to increased

repulsion and hydrophilicity.[60] The current analysis was also important in assessing the MB adsorption mechanism onto surfactant or SAIL sEGO/NFC composites.

The adsorption behaviour of MB onto surfactant or SAIL sEGO/NFC was discussed in detail on the basis of the change in the surface charge demonstrated by ζ-potential, as well as the adsorption isotherm of MB onto sEGO. Considering that all surfactants used were anionic, the zeta potentials were highly negative and became more negative (more stable) by more than 9 mV upon changing the sodium ion to imidazolium ion (Table S7, ESI†). Therefore, the negatively charged adsorbent may have facilitated the electrostatic bonding between MB and the sEGO surface for MB adsorption. Remarkable MB adsorption capacities of the composites were achieved under neutral conditions possibly because of the electrostatic interaction between the dye cation and the negative charged surface of the adsorbent.

Dynamic light scattering (DLS) studies

The particle size and mean diameter of surfactants and surfactants/sEGO were quantified using DLS.[67] DI water is less favourable as a solvent for DLS measurement because the ion-free environment affects the electrostatic particle interactions.[68] The mean diameter of the sodium surfactants was found to be in the range of 1.5–22.6 nm. Exchanging the sodium for BMIM increased the particle size to 35.0–224.0 nm, a significant increase (Table S8, ESI†). Evidently, the nanomaterial aggregate sizes approach the micron scale with the surfactant acting as an efficient stabilizer.[69] According to Bhattacharjee,[65] particle mixtures exceeding 100 nm are not considered as nanomaterials. Therefore, although most samples remained within the nanomaterial size range, the presence of GO resulted in a non-nanomaterial system for those stabilised with SAILs and BMIM-TC14.

Surface tension

Fig. 5 demonstrates how the surface tension of the surfactant solutions and sEGO suspension decreased as a function of surfactant concentration. This finding was followed by a sharp linear decline at intermediate concentrations and displayed a flat region at high concentrations. Before the concentrations where the plateaus appeared, the surface tension of the mixed GO–surfactant systems decreased obviously compared with that of pure surfactant solutions. This finding shows that the presence of GO affected the surface activity of SAIL. The initial concentration of BMIM-TC14 with CMC of 11.7 mM decreased to 11.3 mM for BMIM-TC14 sEGO.[70] BMIM-AOT14 and BMIM-AOT14 sEGO had the same CMC (7.5 mM), whereas BMIM-DS (1.5 mM) and BMIM-DS sEGO (1.2 mM) had a 0.3 mM difference.

Previous research has mentioned that surfactants can reduce the surface energy of water (72.8 mN m^{-1}; unsuitable for graphene exfoliation) during graphite exfoliation to match that of graphite and weaken the interactions (π–π conjugation, Coulomb attraction, and hydrophobic interactions) amongst graphite surfaces,[71] further supporting the surface tension results.

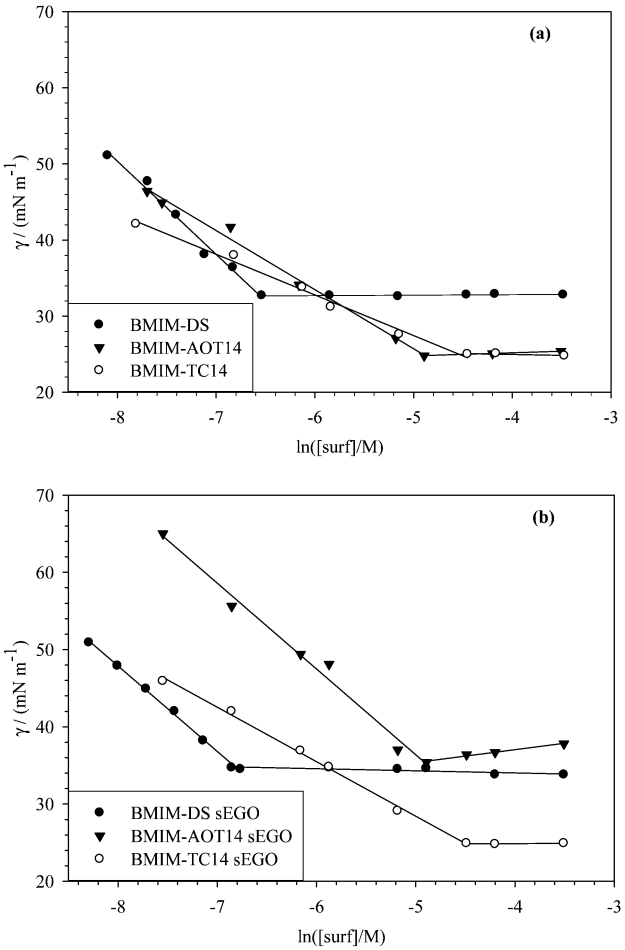

Fig. 5 Air–water surface tension (γ) *vs.* ln(concentration) plots for surfactant solutions (a) and sEGOs (b) at 25 °C.

General observations revealed that the surfactant solutions displayed lower surface tension than the sEGO samples. The hydrophobic groups of surfactants adsorbed onto the basal plane of GO sheets through hydrophobic interactions, whereas the hydrophilic groups oriented towards water. Therefore, water-dispersible GO can be obtained by establishing electrostatic repulsion amongst adjacent GO sheets.[60] A trend of lower surface tension with higher branching of the IL surfactant can also be observed for all SAIL solutions (Table 3). This result implies that the binding mechanisms between SAILs and SAILs (that contain an aromatic group acting as an anchor for surfactant onto GO *via* π–π interactions and Coulomb attractions) differed from each other.[72]

Another important parameter that can be derived from surface-tension measurement is the limiting surface tension (γ_{cmc}), which explains the effectiveness of SAILs to reach the maximum surface-tension reduction.[73,74] A previous publication has reported that TC14 has a lower γ_{cmc} value (25.8 mN m^{-1}) than di-chain (AOT14) and single-chain (SDS) surfactants owing to the highly branched tails in TC14s.[15] In the present study,

Table 3 Parameters derived from surface tension measurements including the fractional free volume (FFV)

Surfactant	CMC (mM) ± 0.03	γ_{cmc} (mN m^{-1}) ± 1	A_{cmc} (Å^2) ± 2	FFV
BMIM-TC14	11.7	25.0	282	0.08
BMIM-TC14 sEGO	11.3	24.9	188	0.12
BMIM-AOT14	7.5	24.8	108	0.21
BMIM-AOT14 sEGO	7.5	35.4	94	0.32
BMIM-DS	1.5	32.7	79	0.24
BMIM-DS sEGO	1.2	34.5	66	0.29

exchanging sodium ion with BMIM on TC14 decreased the surface tension to 25.0 mN m^{-1} (Table 3).[15] The surface tension of AOT14 is reported to be 28.1 mN m^{-1}, whereas that of SDS is 36.1 mN m^{-1}.[15] Changing the sodium into BMIM in AOT14 and SDS interestingly decreased the surface tension by 3.3 and 3.4 mN m^{-1} respectively. These results demonstrate that modifying the surfactant headgroup improves surfactant performance by lowering the cohesive energy density between hydrocarbon tails, causing easier wetting.[75] A lower headgroup area (A_{cmc}) increased the molecular packing parameter (CPP), and the surface area per surfactant molecule was determined by the surfactant headgroup.[76] Evidence remains lacking; however, Ravula *et al.* mentioned that ILs possess surface tension closely matching the surface energy of graphite which makes them an exceptional medium for exfoliation and GO stabilisation.[77] The water–graphite surface tension is estimated to be 32 mN m^{-1}.[78] The surface excesses, Γ, limiting the head-group areas at the CMC, and A_{cmc} were obtained by fitting the pre-CMC data through the Gibbs equation (eqn (8)):

$$\Gamma = -\frac{1}{mRT}\frac{d\gamma}{d\ln c} \quad (8)$$

where m is a pre-factor of 2 for 1 : 1 fully dissociating ions. The effective area per molecule at CMC (A_{cmc}/Å^2) in the adsorbed monolayers can thus be determined through eqn (9):

$$A_{cmc} = \frac{1}{\Gamma N_a} \quad (9)$$

Another important parameter which can be derived from the surface tension data is fractional free volume (FFV) (eqn (10)) that quantifies the 'bulkiness' of the surfactant molecule, as introduced by Stone and his team.[79] V_t is the van der Waals volume of the surfactant tail (an approximation of how much volume the surfactant tails occupy), t_1 is the thickness of the interface, and A_{cmc} is the effective area per molecule.

$$FFV = 1 - \frac{V_t}{t_1 A_{cmc}} \quad (10)$$

It is assumed that a lower value of FFV, which can be directly calculated from the surfactant-tail geometry, provides better stability by decreasing the interfacial tension, reducing the overlap between tails, and increasing the interfacial curvature.[80] Here, BMIM-TC14 provided the lowest FFV. As such, it can be assumed that amongst all SAILs, BMIM-TC14 occupied the largest area at the interface and was thus more effective for stabilisation. In a previous study,[15] TC14 was reported to be the most efficient surfactant with an FFV value of 0.12. Therefore, the modification of the surfactant head structure affects the surfactant interfacial curvature as reflected by the FFV value.

Small-angle neutron scattering (SANS)

SANS allows studies of the shapes and sizes of self-assembled materials, which in this case are surfactant molecules and sEGO sheets in solution. In SANS, the scattered intensity, $I(Q)$, is related to the nanostructures present, where the features contributing to $I(Q)$ are the shape and size of the nanoparticles defined as the particle form factor, $P(Q)$.[79,81] Theoretically, larger particles scatter at smaller Q whereas smaller particles scatter to higher Q.[81] Ionic surfactants interact with graphene by forming a monolayer with the hydrophilic head-group exposed in solution and the hydrophobic part in direct contact with graphene to maximise the strength of van der Waals interactions with the substrate.

Fig. 6 shows the SANS profiles of SAILs and SAILs combined with the exfoliated GO and sEGO. The parameters derived from the SANS profiles are listed in Table 4. A remarkable difference in the scattering profiles was seen for BMIM-TC14 and BMIM-TC14 sEGO. For BMIM-TC14 sEGO the profile was well fitted into the paracrystalline lamellar stack model. BMIM-TC14 also adequately fitted the paracrystalline lamellar stack model but showed lower $I(Q)$ in all Q regions.

The main reason for this phenomenon was the adsorption of SAILs onto GO forming sEGO.[15] However, for BMIM-AOT14 and BMIM-AOT14 sEGO, the scattering was broadly the same. Thus, the bulk micelles were more dominant than those molecules adsorbed onto the GO surfaces, similar to our previous observation on AOT14 samples.[15] However, obvious changes in the bilayer thicknesses (L), separation between bilayers (D), and number of bilayers (M) for BMIM-AOT14 and BMIM-AOT14 sEGO can be seen (Table 4). The increase in colloidal dimensions (surfactant or SAILs in the presence of GO) of GO basal spacing may decrease the attraction between lamellae.[82] Different from BMIM-AOT14 and BMIM-TC14, the SANS data for BMIM-DS adequately fitted a spherical micelle model. The presence of GO did not lead to any micellar shape transitions, but the bump for BMIM-DS sEGO was more pronounced presumably owing to an increase in intermicellar interactions.[15] For linear hydrocarbon molecules, the strength of van der Waals interactions with the substrate scales with chain length, suggesting that a longer carbon chain should have a stronger interfacial affinity and thus a higher graphene-dispersion efficiency.[83] The structure of the surfactant layer is another factor that should influence graphene-dispersion efficiency as evidenced by the differences in the performance of SDS in dispersing carbon nanotubes and graphene.[84] According to Cao,[85] negatively charged polymers such as poly(4-styrenesufonic acid-*co*-maleic acid) sodium salt and poly(diallyldimethylammonium chloride), when mixed with IL, lead to the weakening of hydrophobic interactions in the surfactant

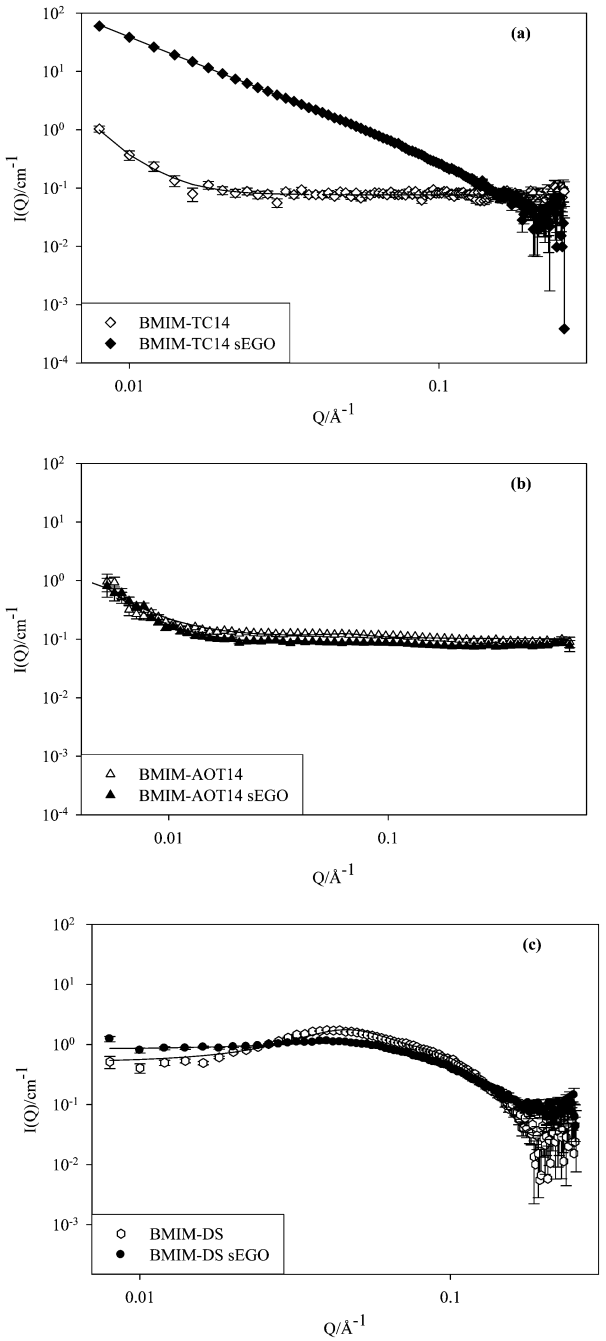

Fig. 6 SANS data for (a) BMIM-TC14 and BMIM-TC14 sEGO, (b) BMIM-AOT14 and BMIM-AOT14 sEGO, and (c) BMIM-SDS and BMIM-SDS sEGO. [Surfactant] = 30 mM (at CMC), and [sEGO] = 0.2 mg mL^{-1} at 25 °C. Lines are model fits for either a paracrystalline lamellar stacked mode or charged spherical micelles (incorporating a Hayter–Penfold $S(Q)$). Characteristic error bars are shown for the lowest intensity samples.

tails. This finding is owing to the strong electrostatic attraction between the polymers and surfactants, thereby reducing the electrostatic repulsion between the surfactant headgroups. However, the neutral polymer used here, which is NFC, exhibited weaker electrostatic interactions with the IL which showed no effects, indicating that it did not affect the CMC, adsorbed amount (Γ_{max}), and aggregation number (N_{agg}). Thus, micellisation was unaffected.

Proposed mechanism

A previous publication has covered the applications of exfoliating graphite in a mixture of surfactants or SAILs and nanocellulose for the development of graphene/cellulose conductive composites.[25] The intercalation of anionic surfactant between the interlayers of graphite promotes graphite oxidation, and thus the exfoliation process occurs driven by hydrophobic interactions and hydrogen bonding.[82] The roles of surfactants and SAILs in cellulose solvation and dissolution for surface modification were also considered.[22] The optimum concentration of electrolyte (surfactant or SAILs) leads to sufficient negative charges and electrostatic repulsion between surfactant and cellulose, thereby promoting stability of the cellulose suspension.[23] Hydrophobic interactions induced by anionic surfactant tails enhance the affinity with the NFC cellulosic surfaces.[86] A 0.05 M concentration of electrolyte was selected as this is the optimum value in producing GO along with 7 V sufficient for graphite exfoliation.[25,87] Details of the mechanism of electrochemically exfoliated graphite by surfactant can be found elsewhere.[15] Here, a mechanism considering the modification of the surfactant headgroup structure with the SAILs used as the electrolyte in the presence of NFC is shown in Fig. 7. Intermolecular hydrogen bonding and π–π stacking by BMIM-TC14 originate from the imidazolium moieties forming bilayer stacks, which may become permanently enlarged.[88] As mentioned earlier, exchanging sodium ions for organic BMIM leads to a decrease in the headgroup area (A_{cmc}) and FFV value, which is also consistent with increasing molecular packing parameter (CPP). Understanding the mechanism helps identify principal factors affecting adsorption. Considering the intrinsic charge and structure of the adsorbent and adsorbate, the adsorption of MB into sEGO could be attributed to electrostatic attraction.[89] Recalling the isotherm studies, MB adsorption onto BMIM-TC14 sEGO/NFC followed the Langmuir and Freundlich models, with a maximum adsorption capacity of 79.4 mg g^{-1} in 15 ppm MB. The fitting of both models suggested that monolayer and multilayer adsorption occurred during the process. Meanwhile, the other composites were better fitted by the Freundlich model. This indicates that the multilayer adsorption of MB molecules onto sEGO/NFC composites may dominate and is favoured over monolayers only. Hence, the BMIM-TC14 sEGO/NFC composites are an effective adsorbent for MB.

According to Ho, Ng, and McKay,[90] MB adsorption into adsorbents can be attributed to the following three principal steps: (1) external diffusion, *i.e.*, the transport of the adsorbate from the bulk phase to the external surface of the adsorbent; (2) intraparticle diffusion involving the transport of the adsorbate from the external surface into the pores, and (3) surface reaction where the adsorbate adheres onto the internal surfaces of the adsorbent. External and intraparticle diffusion are categorised as transport steps, whereas the other is a surface reaction (adsorption) step. GO and its composites have

Table 4 Model fit parameters for SANS data

Sample	Model	R_{sphere} (Å)	L^a (Å)	D^a (Å)	M^a
SAIL solution					
BMIM-DS	Sphere	25.0	—	—	—
BMIM-AOT14	Paracrystalline lamellar stack	—	6.0	69.0	103
BMIM-TC14	Paracrystalline lamellar stack	—	21.0	250.0	21
sEGO					
BMIM-DS sEGO	Sphere	25.0	—	—	—
BMIM-AOT14 sEGO	Paracrystalline lamellar stack	—	11.0	83.0	149
BMIM-TC14 sEGO	Paracrystalline lamellar stack	—	29.0	270.0	30

[a] For lamellar only, where L = thickness of bilayers; D = space between bilayers; and M = number of bilayers.

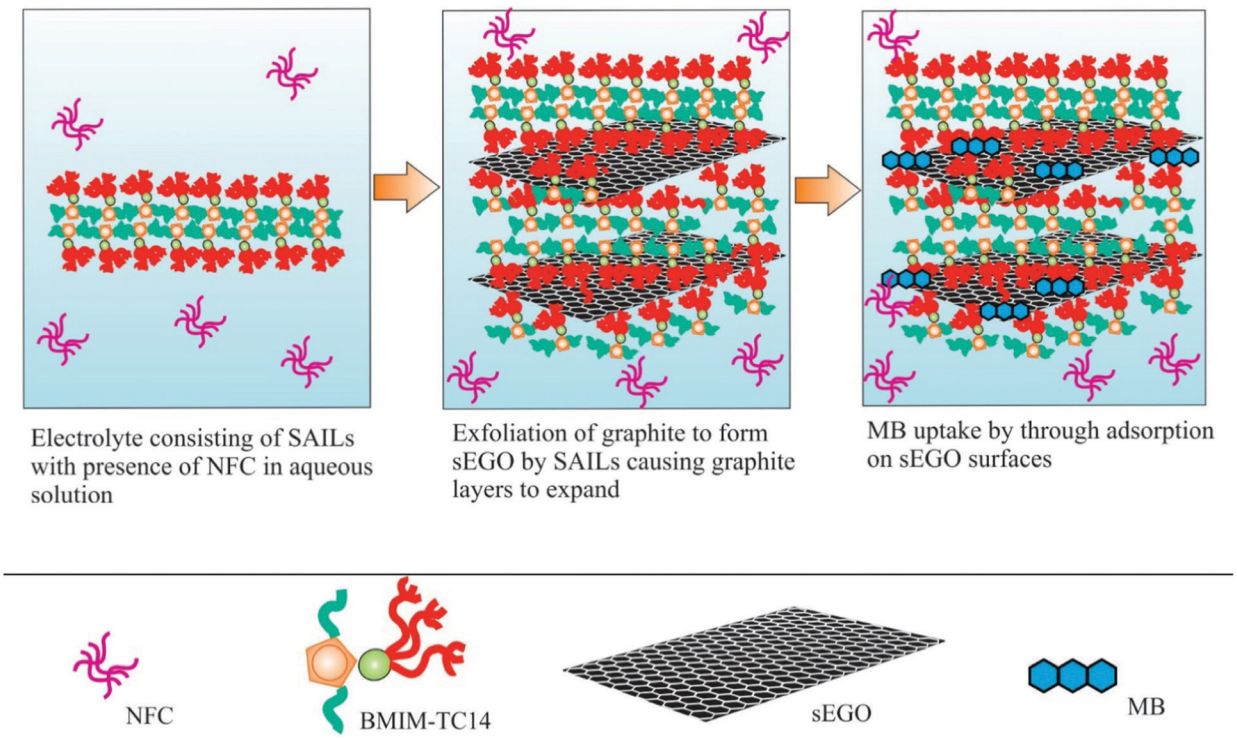

Fig. 7 Schematic (not to scale) of SAIL-mediated graphite exfoliation to form sEGO/NFCs and the adsorption of methylene blue.

abundant hydroxyl, carboxyl, and epoxy groups on the two-dimensional graphene framework surfaces, resulting in strong interactions with organic dyes. The adsorption of organic dyes onto GO-based materials is primarily driven by three interactions, namely, electrostatic (H-bonding), π–π stacking and van der Waals.[10,52,91] The van der Waals interactions represent attractions between single layers of GO sheets[13,92] and are clearly important in this work. MB is a known cationic dye that can interact *via* electrostatic interactions with the negatively charged sEGO composites. Apart from electrostatic interactions, π–π interactions between the aromatic moieties of MB and the hexagonal arrays of carbon atoms in GO may also occur during adsorption.[62] Owing to their dual nature, the surfactants adsorb and accumulate onto the GO surfaces through hydrophobic interactions with their hydrophilic parts orienting towards the aqueous phase. Hu *et al.*,[82] also suggested that anionic surfactants intercalate between the GO interlayers by hydrophobic interactions and hydrogen bonding, resulting in weak electrostatic repulsions between surfactant–GO sheets. Considering that the concentration of the surfactants used was above the CMC, the surfactant micelles may aggregate on the GO surfaces. This phenomenon provides additional functional groups and may further enhance the overall performance of the adsorbents.

A small amount of the MB ions adsorbed onto the sEGO cellulose composites through physical adsorption and electrostatic interactions *via* oxygen-containing functional groups such as hydroxyls and carboxyls. Electrostatic interactions between the sulfate anions (from the anionic head group of the surfactant) which attached perpendicularly to sEGO and the cationic groups in MB may also take place.

Conclusion

Extending previous work,[15] adsorption of a model pollutant dye, MB, has been studied with modified surfactant sEGO modified cellulose composites. GO was obtained through the electrochemical exfoliation of graphite by using a mixture of a custom-made surfactant or SAILs and nanocellulose. This straightforward and economical route enables direct casting of the exfoliated mixture, yielding surfactant or SAIL sEGO/NFC composites. A remarkable 99% removal of MB was achieved with the BMIM-TC14 sEGO/NFC composite, and a maximum adsorption capacity of MB was 74.3 mg g^{-1}. The equilibrium adsorption isotherm could be fitted with Langmuir and Freundlich models, and for the BMIM-TC14 sEGO/NFC composite the adsorption kinetics fitted best a pseudo-second-order model. The strong adsorption capability of sEGO/NFC may have been due to the extensively oxygenated functional groups of sEGO which are available for electrostatic interaction and hydrogen bonding. The presence of surfactant or SAILs on the surface of GO assisted the graphite-exfoliation process, stabilised the colloidal structure of the sEGO composites, and improved their adsorption properties. Remarkably, modifying the surfactant head group by changing the normal sodium ion with the organic cation BMIM, to form SAILs, gave rise to improved absorbents. Evidently, the surfactant/SAIL chemical structure is a crucial factor influencing the performance of these adsorbents. In addition, although the composites applied in this study did not offer 100% removal efficiency, or display the highest adsorption capacity compared to those found in the literature,[14,43–45] significant dye removal can be achieved at relatively low sEGO/NFC composite levels (5 mg). This simple yet efficient method for producing composite graphene oxide-based materials containing surfactants and SAILs provides new insights into their applications as adsorbents in wastewater treatment.

Conflicts of interest

There are no conflicts to declare.

Acknowledgements

This work was funded through a grant from NEWTON FUND: Use of the ISIS Neutron and Muon Source (Grant Code: 2019-0257-103-11). This project was also supported by JSPS [KAKENHI, Grant-in-Aid for Young Scientists (A), No. 23685034] and Leading Research Organizations (RCUK [through EPSRC EP/I018301/1], ANR[13-G8ME0003]) under the G8 Research Councils Initiative for Multi-lateral Research Funding—G8-2012. The authors thank the Science and Technology Facilities Council for the allocation of beam time, travel and consumables (experiment number RB1710004). This work benefited from the use of the SasView application, originally developed under NSF Award DMR-0520547. SasView also contains code developed with funding from the EU Horizon2020 programme under the SINE2020 project Grant No. 654000.

Notes and references

1 S. Song, Y. Ma, H. Shen, M. Zhang and Z. Zhang, *RSC Adv.*, 2015, **5**, 27922–27932.
2 J. A. González, M. E. Villanueva, L. L. Piehl and G. J. Copello, *Chem. Eng. J.*, 2015, **280**, 41–48.
3 V. K. Gupta, I. Ali, T. A. Saleh, A. Nayak and S. Agarwal, *RSC Adv.*, 2012, **2**, 6380–6388.
4 M. T. Yagub, T. K. Sen, S. Afroze and H. M. Ang, *Adv. Colloid Interface Sci.*, 2014, **209**, 172–184.
5 N. Baig, M. Sajid and A. Saleh, *J. Environ. Manage.*, 2019, **244**, 370–382.
6 A. Pourjavadi, M. Nazari, B. Kabiri, S. H. Hosseini and C. Bennett, *RSC Adv.*, 2016, **6**, 10430–10437.
7 Y. Guo, J. Deng, J. Zhu, X. Zhou and R. Bai, *RSC Adv.*, 2016, **6**, 82523–82536.
8 D. R. Dreyer, S. Park, C. W. Bielawski and R. S. Ruoff, *Chem. Soc. Rev.*, 2010, **39**, 228–240.
9 K. Haubner, J. Murawski, P. Olk, L. M. Eng, C. Ziegler, B. Adolphi and E. Jaehne, *ChemPhysChem*, 2010, **11**, 2131–2139.
10 G. K. Ramesha, A. V. Kumara, H. B. Muralidhara and S. Sampath, *J. Colloid Interface Sci.*, 2011, **361**, 270–277.
11 H. Yan, H. Wu, K. Li, Y. Wang, X. Tao, H. Yang, A. Li and R. Cheng, *ACS Appl. Mater. Interfaces*, 2015, **7**, 6690–6697.
12 X. Wei, T. Huang, J. H. Yang, N. Zhang, Y. Wang and Z. W. Zhou, *J. Hazard. Mater.*, 2017, **335**, 28–38.
13 S. Stankovich, D. A. Dikin, R. D. Piner, K. A. Kohlhaas, A. Kleinhammes, Y. Jia, Y. Wu, S. T. Nguyen and R. S. Ruoff, *Carbon*, 2007, **45**, 1558–1565.
14 L. Chen, Y. Li, S. Hu, J. Sun, Q. Du, X. Yang, Q. Ji, Z. Wang, D. Wang and Y. Xia, *J. Exp. Nanosci.*, 2016, **11**, 1156–1170.
15 N. A. Jamaluddin, A. Mohamed, S. A. Bakar, T. Ardyani, M. Sagisaka, S. Suhara, M. H. Mamat, M. K. Ahmad, S. M. King and S. E. Rogers, *et al.*, *Phys. Chem. Chem. Phys.*, 2020, **22**, 12732–12744.
16 A. A. Nayl, A. I. Abd-Elhamid, M. A. Abu-Saied, A. A. El-Shanshory, H. M. A. Soliman, M. A. Akl and H. F. Aly, *RSC Adv.*, 2020, **10**, 7791–7802.
17 M. A. S. Azizi Samir, F. Alloin and A. Dufresne, *Biomacromolecules*, 2005, **6**, 612–626.
18 D. Roy, M. Semsarilar, J. T. Guthrie and S. Perrier, *Chem. Soc. Rev.*, 2009, **38**, 2046–2064.
19 R. J. Moon, A. Martini, J. Nairn, J. Simonsen and J. Youngblood, *Chem. Soc. Rev.*, 2011, **40**, 3941–3994.
20 A. Tshikovhi, S. B. Mishra and A. K. Mishra, *Int. J. Biol. Macromol.*, 2020, **152**, 616–632.
21 B. Lindman, G. Karlström and L. Stigsson, *J. Mol. Liq.*, 2010, **156**, 76–81.
22 D. L. Minnick, R. A. Flores, M. R. Destefano and A. M. Scurto, *J. Phys. Chem. B*, 2016, **120**, 7906–7919.
23 B. L. Tardy, S. Yokota, M. Ago, W. Xiang, T. Kondo, R. Bordes and O. J. Rojas, *Curr. Opin. Colloid Interface Sci.*, 2017, **29**, 57–67.
24 N. Liu, F. Luo, H. Wu, Y. Liu, C. Zhang and J. Chen, *Adv. Funct. Mater.*, 2008, **18**, 1518–1525.
25 A. Mohamed, T. Ardyani, S. A. Bakar, M. Sagisaka, Y. Umetsu, M. R. M. Hussin, M. K. Ahmad, M. H. Mamat,

S. King and A. Czajka, *et al.*, *Carbohydr. Polym.*, 2018, **201**, 48–59.
26 G. Singh, G. Singh and T. S. Kang, *J. Phys. Chem. B*, 2016, **120**, 1092–1105.
27 M. Kaur, G. Singh, K. Damarla, G. Singh, H. Wang, J. Wang, V. K. Aswal, A. Kumar and T. S. Kang, *Phys. Chem. Chem. Phys.*, 2020, **22**, 169–178.
28 T. Li, N. Li, J. Liu, K. Cai, M. F. Foda, X. Lei and H. Han, *Nanoscale*, 2015, **7**, 659–669.
29 Y. Sun, H. Zheng, C. Wang, M. Yang, A. Zhou and H. Duan, *Nanoscale*, 2016, **8**, 1523–1534.
30 D. Krishnan, F. Kim, J. Luo, R. Cruz-Silva, L. J. Cote, H. D. Jang and J. Huang, *Nano Today*, 2012, **7**, 137–152.
31 A. M. Abdelkader, A. J. Cooper, R. A. W. Dryfe and I. A. Kinloch, *Nanoscale*, 2015, **7**, 6944–6956.
32 C. H. Chang and E. I. Franses, *Colloids Surf., A*, 1995, **100**, 1–45.
33 A. Czajka, G. Hazell and J. Eastoe, *Langmuir*, 2015, **31**, 8205–8217.
34 T. M. McCoy, S. A. Holt, A. M. Rozario, T. D. M. Bell and R. F. Tabor, *Adv. Mater. Interfaces*, 2017, **4**, 1–12.
35 A. Y. W. Sham and S. M. Notley, *J. Environ. Chem. Eng.*, 2018, **6**, 495–504.
36 D. T. Ogunleye, S. O. Akpotu and B. Moodley, *Environ. Technol. Innovation*, 2020, **17**, 100616.
37 J. Bowers, C. P. Butts, P. J. Martin, M. C. Vergara-Gutierrez and R. K. Heenan, *Langmuir*, 2004, **20**, 2191–2198.
38 T. Singh and A. Kumar, *J. Phys. Chem. B*, 2007, **111**, 7843–7851.
39 B. Dong, N. Li, L. Zheng, L. Yu and T. Inoue, *Langmuir*, 2007, **23**, 4178–4182.
40 A. Mohamed, K. Trickett, S. Y. Chin, S. Cummings, M. Sagisaka, L. Hudson, S. Nave, R. Dyer, S. E. Rogers and R. K. Heenan, *et al.*, *Langmuir*, 2010, **26**, 13861–13866.
41 A. Mohamed, A. K. Anas, S. A. Bakar, A. A. Aziz, M. Sagisaka, P. Brown, J. Eastoe, A. Kamari, N. Hashim and I. M. Isa, *Colloid Polym. Sci.*, 2014, **292**, 3013–3023.
42 P. Brown, C. P. Butts, J. Eastoe, D. Fermin, I. Grillo, H. Lee, D. Parker, D. Plana and R. M. Richardson, *Langmuir*, 2012, **28**, 2502–2509.
43 Z. Wang, L. Song, Y. Wang, X. Zhang and J. Yao, *J. Phys. Chem. Solids*, 2020, **150**, 109839.
44 K. Kaur, R. Jindal and Meenu, *Carbohydr. Polym.*, 2019, **225**, 115245.
45 F. Ren, Z. Li, W. Tan, X. Liu, Z. Sun, P. Ren and D. Yan, *J. Colloid Interface Sci.*, 2018, **532**, 58–67.
46 S. Senthilkumaar, P. R. Varadarajan, K. Porkodi and C. V. Subbhuraam, *J. Colloid Interface Sci.*, 2005, **284**, 78–82.
47 I. Langmuir, *J. Am. Chem. Soc.*, 1918, **9**, 1361–1403.
48 H. Freundlich, *J. Phys. Chem.*, 1906, **57**, 1100–1107.
49 Y. S. Ho and G. McKay, *Process Saf. Environ. Prot.*, 1998, **76**, 183–191.
50 T. Vincent, J. M. Taulemesse, A. Dauvergne, T. Chanut, F. Testa and E. Guibal, *Carbohydr. Polym.*, 2014, **99**, 517–526.
51 K. L. Tan and B. H. Hameed, *J. Taiwan Inst. Chem. Eng.*, 2017, **74**, 25–48.
52 Y. Qi, M. Yang, W. Xu, S. He and Y. Men, *J. Colloid Interface Sci.*, 2017, **486**, 84–96.
53 D. Qin, Z. Liu, H. Bai and D. D. Sun, *J. Mater. Chem. A*, 2017, **5**, 12183–12192.
54 J. Su, S. He, Z. Zhao, X. Liu and H. Li, *Colloids Surf., A*, 2018, **554**, 227–236.
55 C. Mattevi, G. Eda, S. Agnoli, S. Miller, K. A. Mkhoyan, O. Celik, D. Mastrogiovanni, G. Granozzi, E. Garfunkel and M. Chhowalla, *Adv. Funct. Mater.*, 2009, **19**, 2577–2583.
56 F. Kim, L. J. Cote and J. Huang, *Adv. Mater.*, 2010, **22**, 1954–1958.
57 A. C. Ferrari and J. Robertson, *Phys. Rev. B: Condens. Matter Mater. Phys.*, 2001, **64**, 1–13.
58 M. S. Dresselhaus, A. Jorio, M. Hofmann, G. Dresselhaus and R. Saito, *Nano Lett.*, 2010, **10**, 751–758.
59 T. Skaltsas, X. Ke, C. Bittencourt and N. Tagmatarchis, *J. Phys. Chem. C*, 2013, **117**, 23272–23278.
60 K. Zhang, X. Zhang, H. Li, X. Xing, L. Jin, Q. Cao and P. Li, *J. Mater. Sci.*, 2018, **53**, 2484–2496.
61 Y. Zhu, S. Murali, W. Cai, X. Li, J. W. Suk, J. R. Potts and R. S. Ruoff, *Adv. Mater.*, 2010, **22**, 3906–3924.
62 M. Yusuf, M. A. Khan, M. Otero, E. C. Abdullah, M. Hosomi, A. Terada and S. Riya, *J. Colloid Interface Sci.*, 2017, **493**, 51–61.
63 M. Kaszuba, J. Corbett, F. M. N. Watson and A. Jones, *Philos. Trans. R. Soc., A*, 2010, **368**, 4439–4451.
64 P. Kumar and H. B. Bohidar, *Colloids Surf., A*, 2010, **361**, 13–24.
65 S. Bhattacharjee, *J. Controlled Release*, 2016, **365**, 337–351.
66 S. Park and R. S. Ruoff, *Nat. Nanotechnol.*, 2009, **4**, 217–224.
67 A. Ali, V. Bhushan, N. A. Malik and K. Behera, *Colloid J.*, 2013, **75**, 357–365.
68 J.-L. B. Eric Farrell, *Guide for DLS sample preparation*, 2017.
69 T. Kureha, K. Hayashi, X. Li and M. Shibayama, *Soft Matter*, 2020, **16**, 10946–10953.
70 F. Zhang, S. Li, Q. Zhang, J. Liu, S. Zeng, M. Liu and D. Sun, *J. Mol. Liq.*, 2019, **276**, 338–346.
71 A. Ciesielski and P. Samorì, *Chem. Soc. Rev.*, 2014, **43**, 381–398.
72 L. Zhang, Z. Zhang, C. He, L. Dai, J. Liu and L. Wang, *ACS Nano*, 2014, **8**, 6663–6670.
73 J. Eastoe, A. Paul, A. Downer, D. C. Steytler and E. Rumsey, *Langmuir*, 2002, **18**, 3014–3017.
74 M. J. Rosen, *Surfactants and interfacial phenomena*, vol. 40, 2004.
75 A. Mohamed, M. Sagisaka, M. Hollamby, S. E. Rogers, R. K. Heenan, R. Dyer and J. Eastoe, *Langmuir*, 2012, **28**, 6299–6306.
76 R. Nagarajan, *Langmuir*, 2002, **18**, 31–38.
77 S. Ravula, S. N. Baker, G. Kamath and G. A. Baker, *Nanoscale*, 2015, **7**, 4338–4353.
78 A. Pertsin and M. Grunze, *J. Phys. Chem. B*, 2004, **108**, 1357–1364.
79 M. T. Stone, P. G. Smith, S. R. P. Rocha, P. J. Rossky and K. P. Johnston, *J. Phys. Chem. B*, 2004, **108**, 1962–1966.
80 C. Hill, Y. Umetsu, K. Fujita, T. Endo, K. Sato, A. Yoshizawa, S. E. Rogers, J. Eastoe and M. Sagisaka, *Langmuir*, 2020, **36**, 14829–14840.
81 M. J. Hollamby, *Phys. Chem. Chem. Phys.*, 2013, **15**, 10566–10579.

82 Y. Hu, M. Su, X. Xie, C. Sun and J. Kou, *Appl. Surf. Sci.*, 2019, **494**, 1100–1108.
83 A. Mohamed, T. Ardyani, S. A. Bakar, M. Sagisaka, Y. Umetsu, J. J. Hamon, B. A. Rahim, S. R. Esa, H. P. S. A. Khalil and M. H. Mamat, *et al.*, *J. Colloid Interface Sci.*, 2018, **516**, 34–47.
84 Y. J. Lee, L. Huang, H. Wang, M. L. Sushko, B. Schwenzer, I. A. Aksay and J. Liu, *Colloids Interface Sci. Commun.*, 2015, **8**, 1–5.
85 H. Cao, Y. Hu, W. Xu, Y. Wang and X. Guo, *J. Mol. Liq.*, 2020, **319**, 114354.
86 W. G. Glasser, R. H. Atalla, J. Blackwell, R. M. Brown, W. Burchard, A. D. French, D. O. Klemm and Y. Nishiyama, *Cellulose*, 2012, **19**, 589–598.
87 M. D. Nurhafizah, A. B. Suriani, A. Mohamed and T. Soga, *Diamond Relat. Mater.*, 2020, **101**, 107624.
88 D. F. Evans and H. Winnerstrom, *The Colloidal Domain: Where Physics, Chemistry, Biology, and Technology Meet*, 1994.
89 P. Bradder, S. K. Ling, S. Wang and S. Liu, *J. Chem. Eng. Data*, 2011, **56**, 138–141.
90 Y. S. Ho, J. C. Y. Ng and G. Mckay, *Sep. Purif. Methods*, 2011, **29**, 189–232.
91 S. T. Yang, S. Chen, Y. Chang, A. Cao, Y. Liu and H. Wang, *J. Colloid Interface Sci.*, 2011, **359**, 24–29.
92 C. Wang and H. Morgner, *Phys. Chem. Chem. Phys.*, 2014, **16**, 23386–23393.

